Supporting Information

Facile Fabrication of Foldable Electrospun Polyacrylonitrile-Based Carbon Nanofibers for Flexible Lithium-Ion Batteries

Renzhong Chen, Yi Hu, Zhen Shen, Peng Pan, Xia He, Keshi Wu, Xiangwu Zhang, and Zhongling Cheng*

*E-mail: huyi-v@zstu.edu.cn

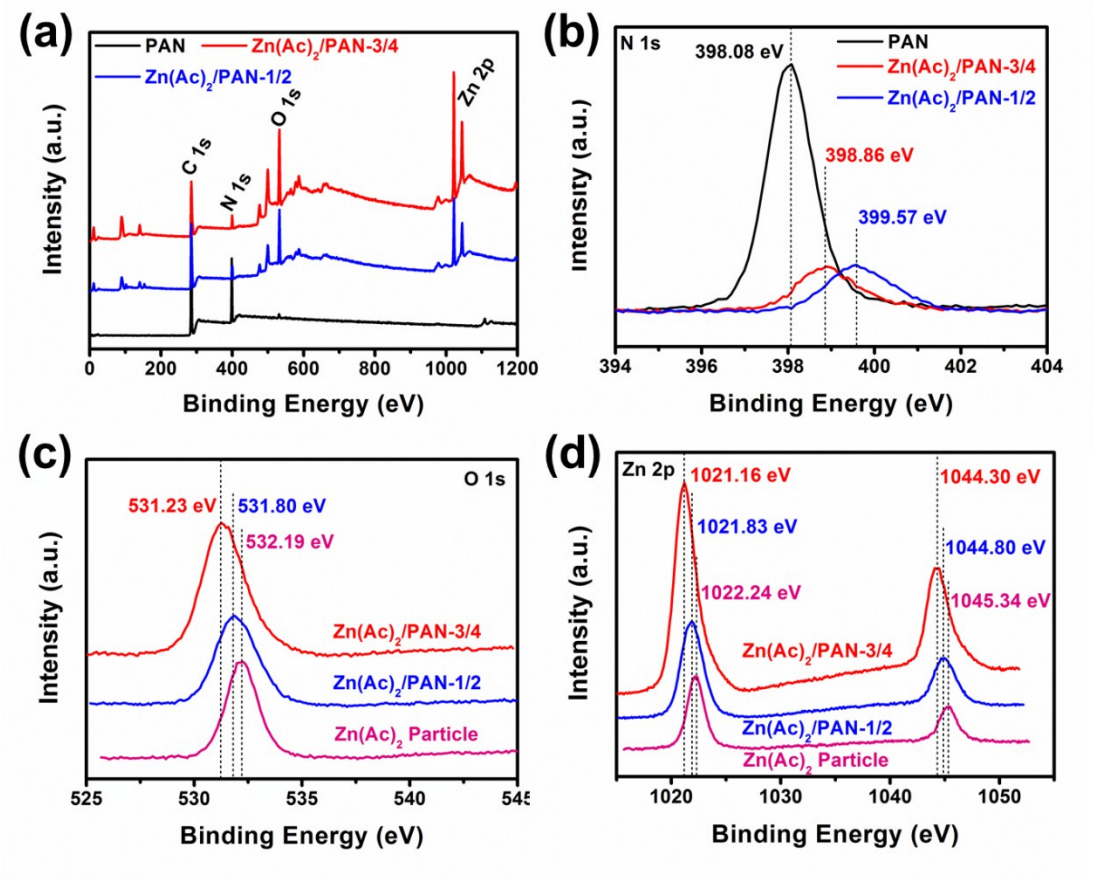

Fig. S1 XPS spectra of $Zn(Ac)_2$ nanoparticles, PAN nanofibers, and $Zn(Ac)_2$/PAN nanofibers: a) survey spectrum and b) N 1s, c) O 1s, and d) Zn 2p spectra. The chemical bonding states of $Zn(Ac)_2$/PAN nanofibers were investigated by XPS. The full wide-scan spectrum exhibits strong O and Zn signals from the $Zn(Ac)_2$/PAN nanofibers, confirming the presence of

$Zn(Ac)_2$. The high-resolution N 1s spectrum shows that the peaks of the N atoms in the $Zn(Ac)_2$/PAN nanofibers shift to higher bonding energies, indicating that they lose electrons. The bonding energy of the N atoms in the $Zn(Ac)_2$/PAN-1/2 nanofibers is higher than that of the N atoms in the $Zn(Ac)_2$/PAN-3/4 nanofibers, indicating that more electrons are lost by the N atoms in the $Zn(Ac)_2$/PAN-1/2 nanofibers. Meanwhile, the O 1s and Zn 2p peaks shift to lower bonding energies, since the O atoms gain electrons and the Zn atoms lose electrons, respectively. However, the bonding energies of the O and Zn atoms in the $Zn(Ac)_2$/PAN-3/4 nanofibers are lower than they are in the $Zn(Ac)_2$/PAN-1/2 nanofibers, unlike the binding energies of the N atoms, which is attributable to the formation of O–Zn bonds between neighboring $Zn(Ac)_2$ salt molecules in the $Zn(Ac)_2$/PAN-3/4 nanofibers. However, in the $Zn(Ac)_2$/PAN-1/2 nanofibers, more N–Zn bonds are formed between the PAN and $Zn(Ac)_2$ salt molecules.

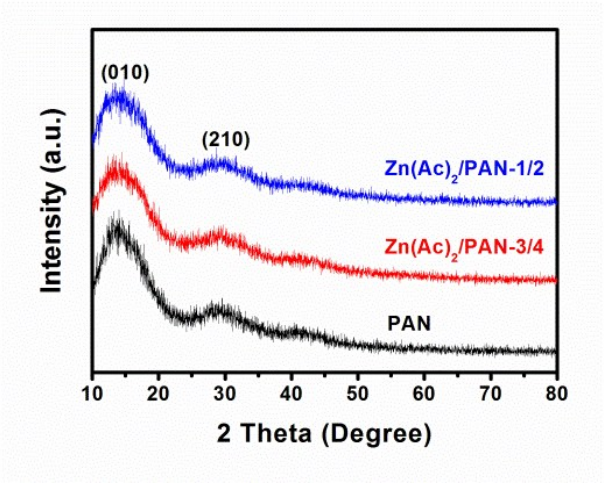

Fig. S2 XRD patterns of $Zn(Ac)_2$/PAN and pristine PAN nanofibers. The peaks at 16° and 28° for the $Zn(Ac)_2$/PAN nanofibers correspond to the (101) and (210) planes, respectively, of PAN and are broader than those of the pristine PAN nanofibers, indicating lower crystallinity.

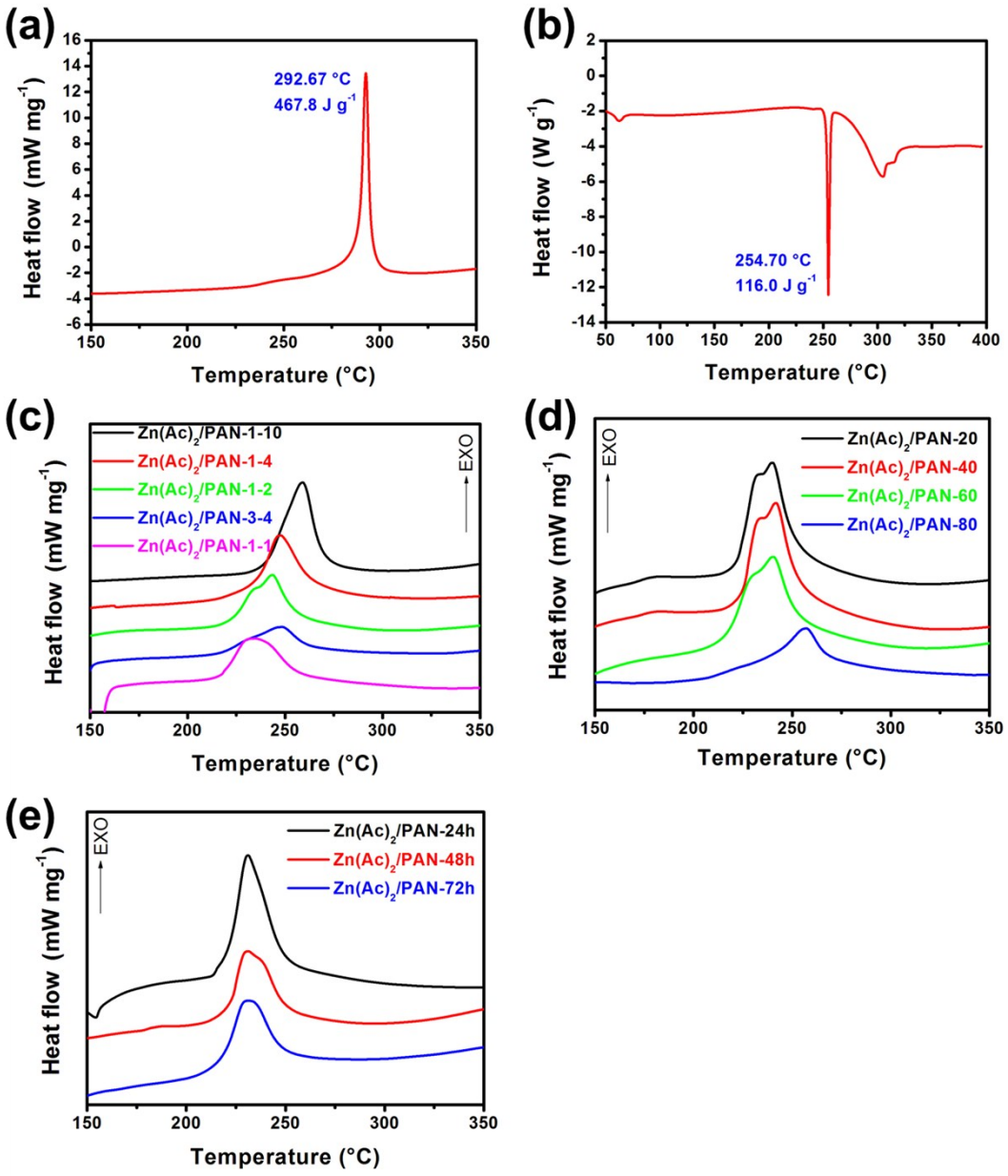

Fig. S3 DSC curves of a) PAN nanofibers, b) $Zn(Ac)_2$ nanoparticles, and $Zn(Ac)_2$/PAN nanofibers fabricated using different c) $Zn(Ac)_2$ contents, d) stirring temperatures, and e) stirring durations (heating rate: 5 °C, in N_2). The pure PAN nanofibers exhibit a single exothermal peak at 292.7 °C related to the cyclization via a radical reaction, while the $Zn(Ac)_2$ nanoparticles display a strong endothermic peak at 254.7 °C corresponding to the melting of $Zn(Ac)_2$. The exothermal peaks related to the cyclization of the $Zn(Ac)_2$/PAN nanofibers shift to a low temperature of around 250 °C and separate into two exothermal peaks corresponding to different thermo-chemical reactions, which could be attributable to the

melting of $Zn(Ac)_2$. The high- and low-temperature exothermal peaks are associated with the ionic and radical reaction mechanisms, respectively. As the $Zn(Ac)_2$ content increases, the initial exothermic peaks shift to lower temperatures, indicating the intensification of the radical reaction. With increasing stirring temperature and duration, the exothermic peaks become broader, indicating the weakening of the radical reaction. Reducing the cyclization temperature and slowing down the exothermic reactions are believed to improve the mechanical properties of the resulting CNFs by reducing the thermal damage incurred by the PAN nanofibers during the stabilization process.[1]

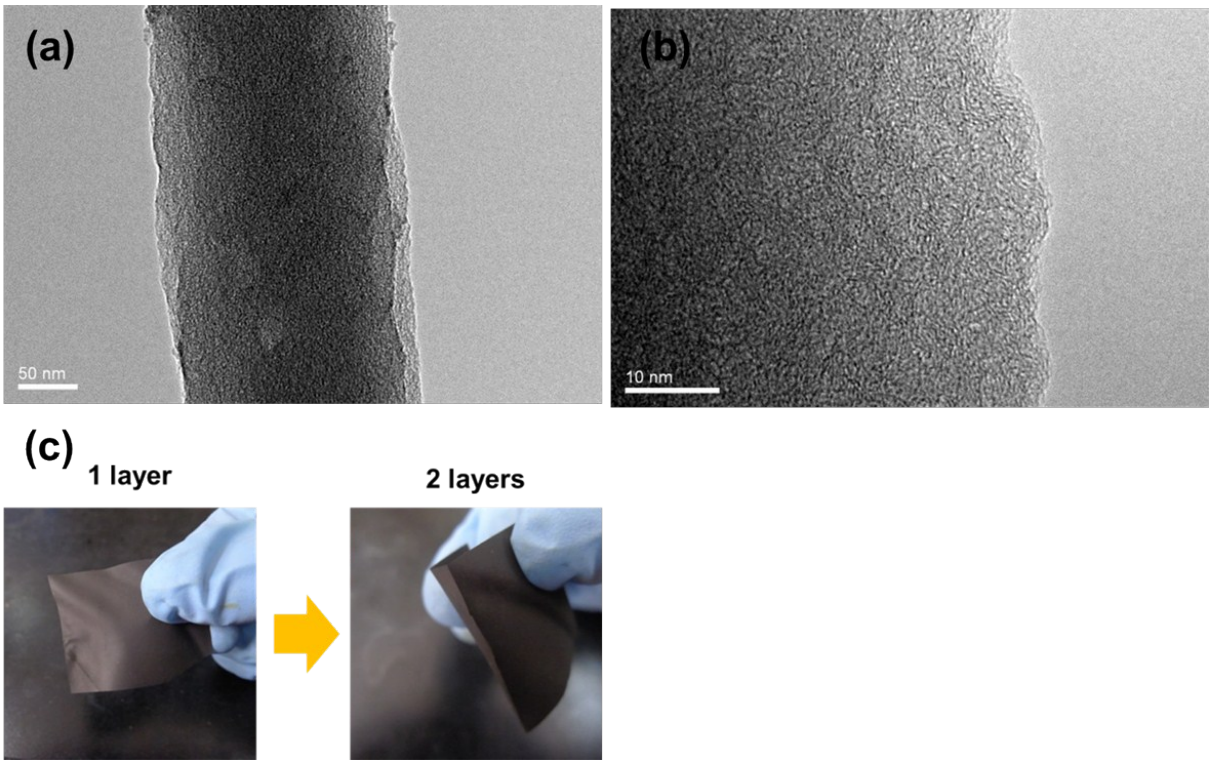

Fig. S4 a) TEM and b) high-resolution TEM (HRTEM) images of the pristine CNF and c) the pristine CNF folding test. Graphite layers are observable in the HRTEM images, and the folding test pictures reveal that the pristine CNFs are brittle.

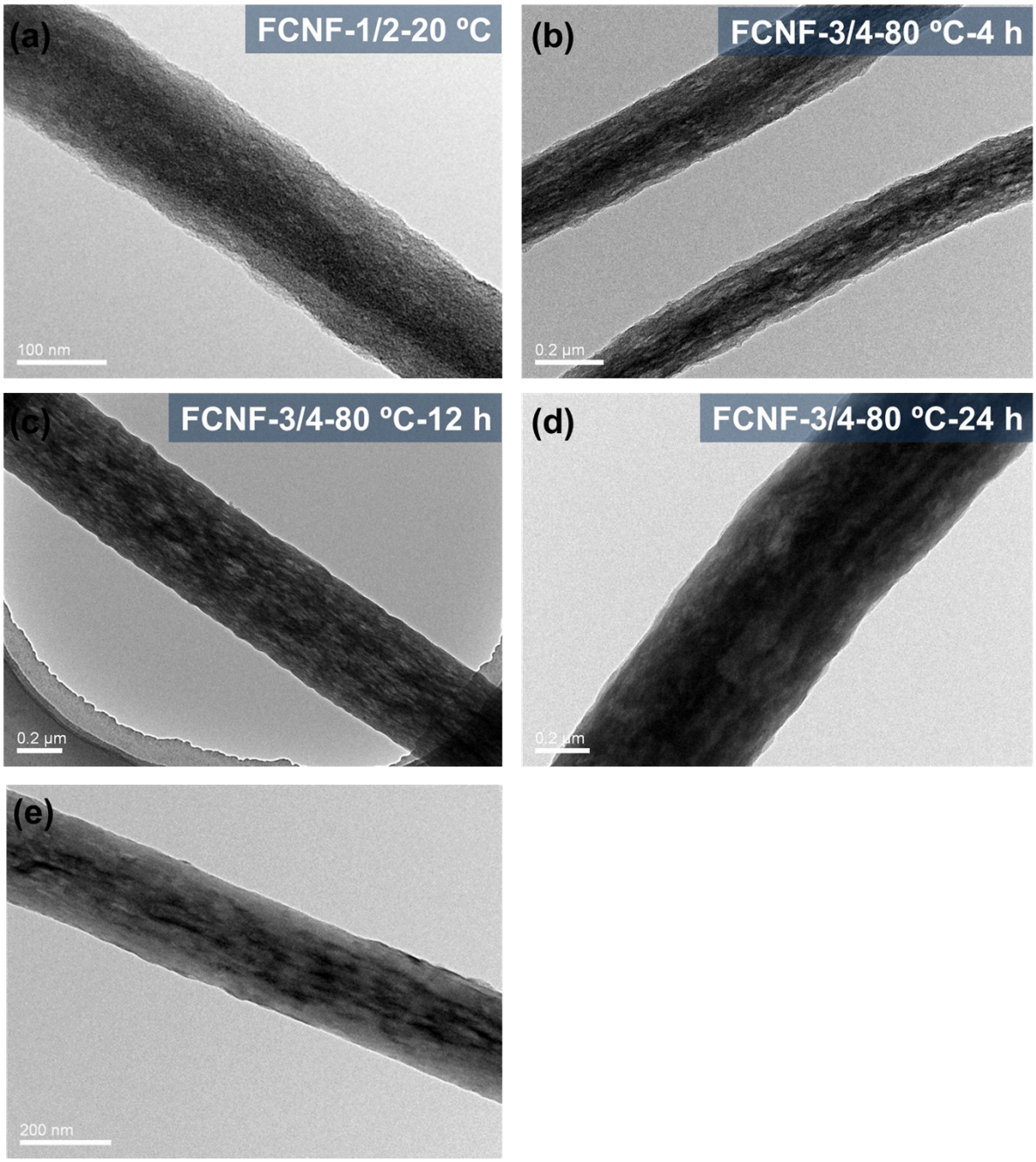

Fig. S5 TEM images of a) FCNF-1/2-20 °C, b) FCNF-3/4-80 °C-4 h, c) FCNF-3/4-80 °C-12 h, d) FCNF-3/4-80 °C-24 h, and e) $Zn(Ac)_2$/PAN nanofibers.

As Fig. S5a shows, FCNF-1/2-20 °C, which was prepared using 0.24 g of $Zn(Ac)_2$ in a spinning solution with stirring for 72 h at 20 °C, exhibits a porous structure, indicating that the $Zn(Ac)_2$ concentration is not the main factor affecting the fiber structure. Meanwhile, **Fig. S5b–d** present TEM images of FCNF-3/4-80 °C-*t*, which was stirred at 80 °C. As the stirring time increases, the shuttle-like mesopores gradually become smaller, indicating that the high

temperature enhances the uniformity of the dispersion of $Zn(Ac)_2$. It should be noted that the number of pores in FCNF-3/4-80 °C-24 h is less than that in FCNF-3/4-80 °C-4 h, suggesting that the mesopores can be partially removed via stirring at a high temperature. The mesopores might be removed completely by stirring for longer at 80 °C or stirring at a higher temperature. In summary, both the mesoporous structure formation and removal can be controlled for FCNF-3/4 and FCNF-1/2, respectively, by changing the stirring temperature.

The dark regions in the nanofiber depicted in **Fig. S5e** are related to the shuttle-like $Zn(Ac)_2$-enriched regions.

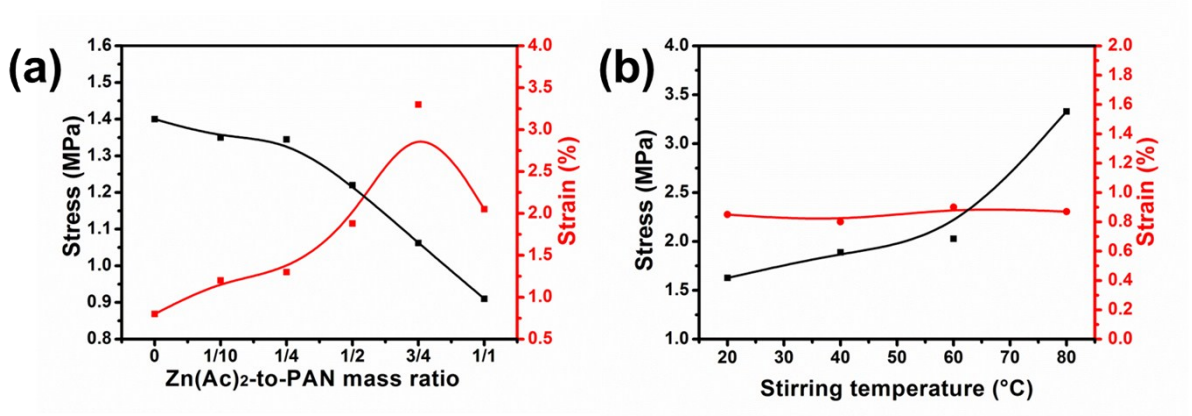

Fig. S6 Mechanical properties of various FCNFs fabricated using different a) $Zn(Ac)_2$ contents (stirring for 72 h at 20 °C) and b) stirring temperatures (0.24 g of $Zn(Ac)_2$ in a spinning solution with stirring for 24 h).

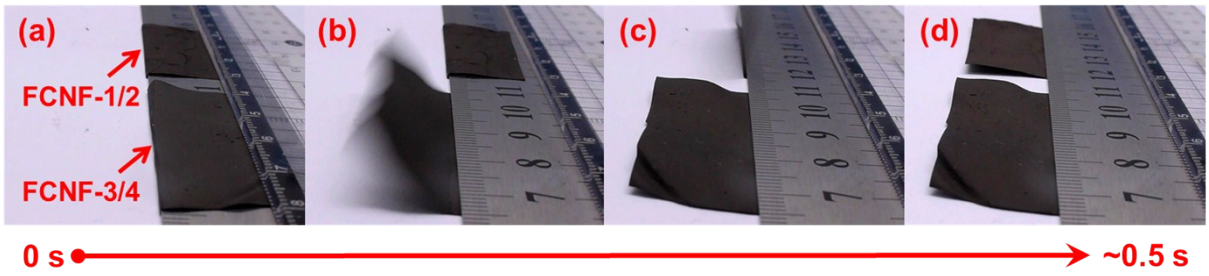

Fig. S7 Digital photos of the recovery performances of the FCNFs.

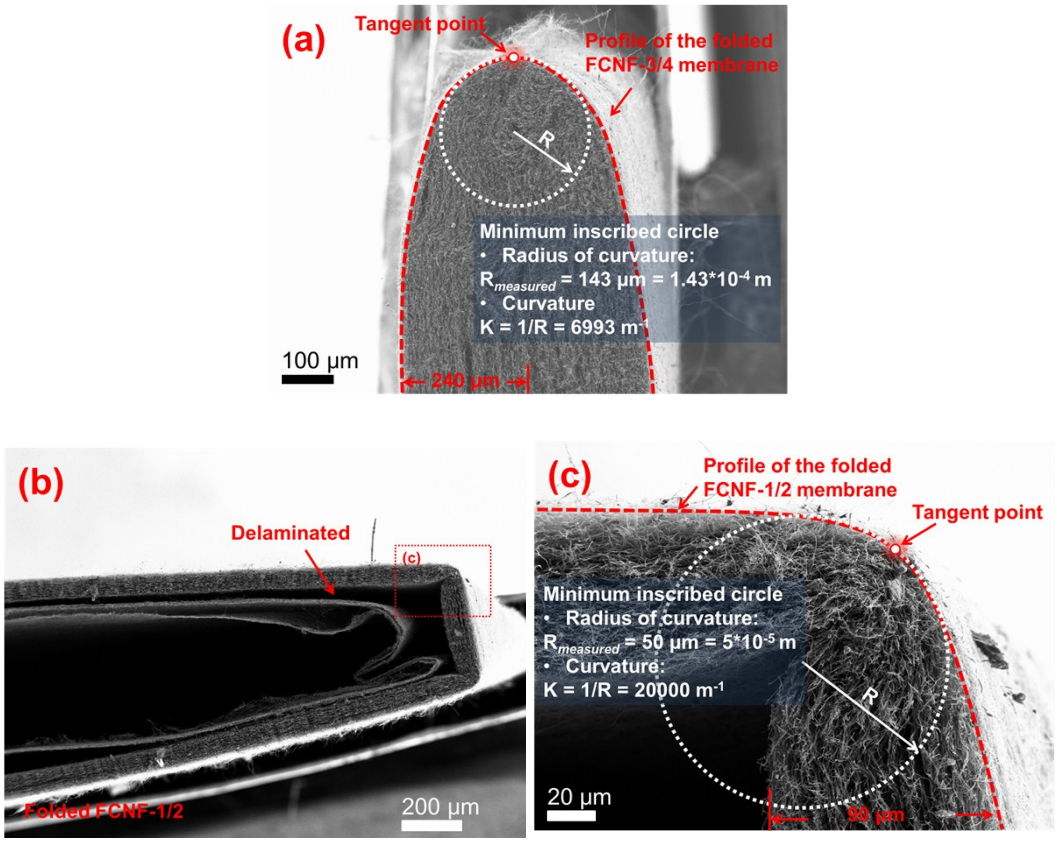

Fig. S8 SEM images of a) FCNF-3/4 and b) FCNF-1/2 when folded with the maximum possible curvature. FCNF-3/4, which was 240 μm thick, could be folded with a bending curvature of 6993 m^{-1}. Although the bending curvature of FCNF-1/2, which was thinner, is larger than that of FCNF-3/4, FCNF-1/2 was delaminated during bending.

Table S1. Comparison of the flexibilities of the FCNFs and previously reported electrospun CNFs.

Material	Precursor	Fiber structure	Bending radius (mm)	Bending angle	Multiple-folding capacity (times)	Ref.
HPCNFs	PAN	Porous	>10	<180°	1	S2
P-CNFs	PAN	Porous	-	=180°	1	S3
TiC/CNF	PAN/ PVP	Porous and nanoparticle loading	-	=180°	1	S4
ZnO/CNF	PAN	Porous and nanoparticle loading	-	=180°	1	S5
SnO_x−ZnO CNF	PAN	Porous and nanoparticle loading	-	=180°	1	S6
SnO_2/CNFs	PBZ	Porous and nanoparticle loading	≈0	=180°	1	S7
SnO_2@ NCNF	PI	Porous and nanoparticle loading	≈2.5	=180°	1	S8
N-CNF	PI	Porous	≈2.5	=180°	1	S9
NCNF	PI	Porous	-	=180°	1	S10
FCNF-3/4	**PAN**	**Porous**	**≈0**	**=180°**	**4**	**Present study**
FCNF-1/2	**PAN**	**Solid**	**≈0**	**=180°**	**4**	**Present study**

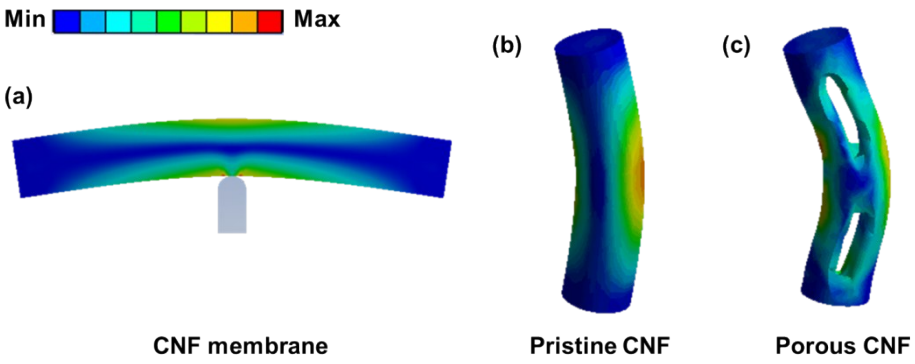

Fig. S9 Stress clouds of a) CNF membrane, b) pristine CNF, and c) porous CNF obtained using the finite element method. With the application of the same load, the porous CNF exhibits greater deformation, and the stress can be distributed around the pores.

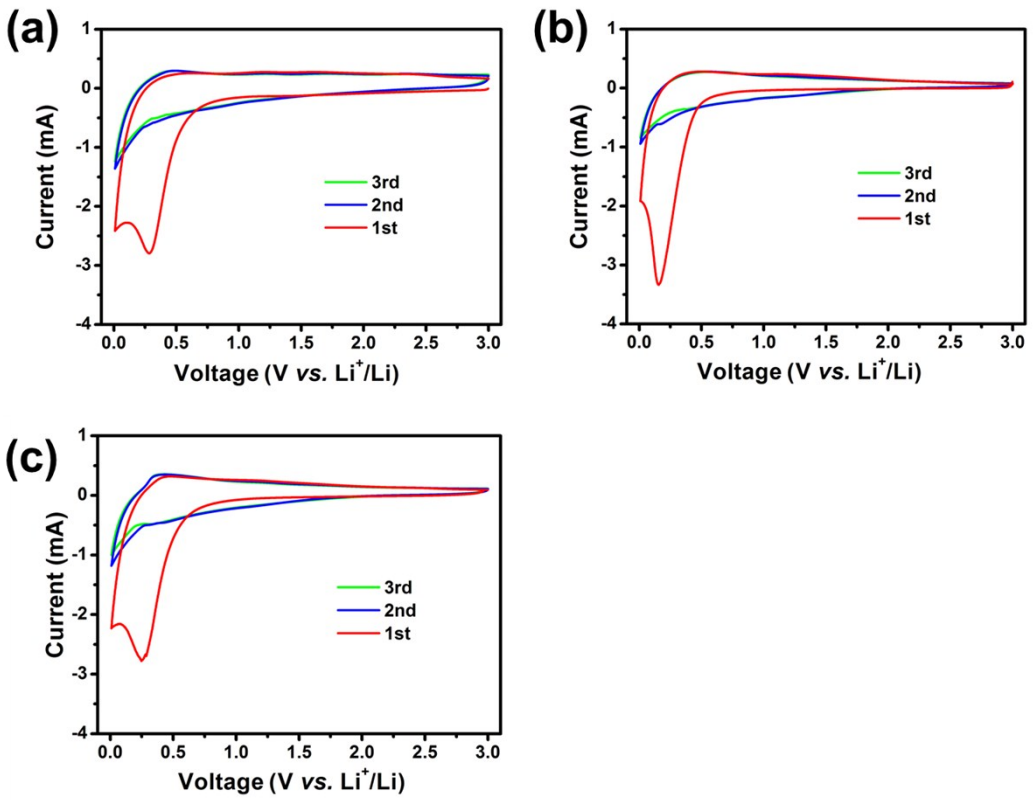

Fig. S10 CV curves for a) FCNF-3/4, b) FCNF-1/2, and c) the pristine CNF.

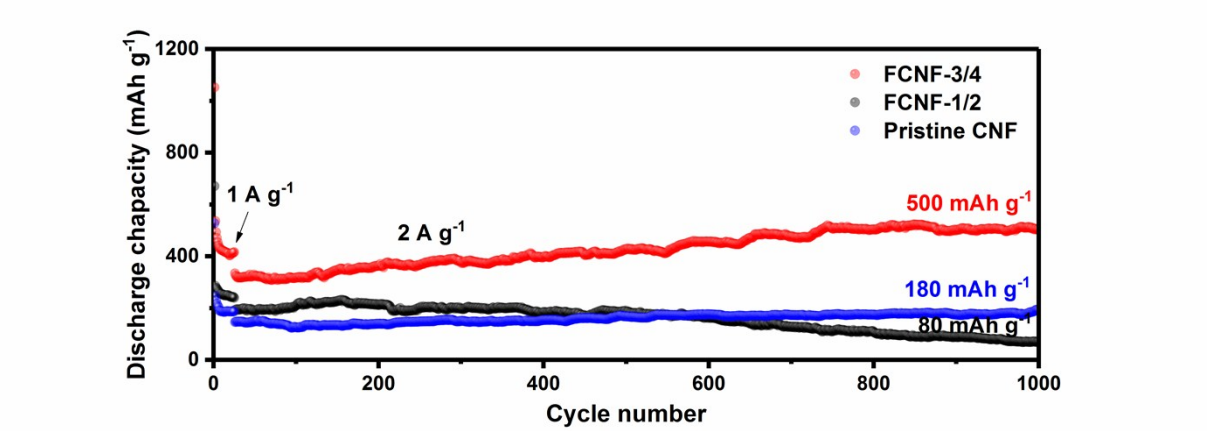

Fig. S11 Long-term cyclic performances of the FCNFs and pristine CNF. The apparent increase in capacity observable for FCNF-3/4 and corresponding to an activation process may result from its large specific surface area and highly porous structure.

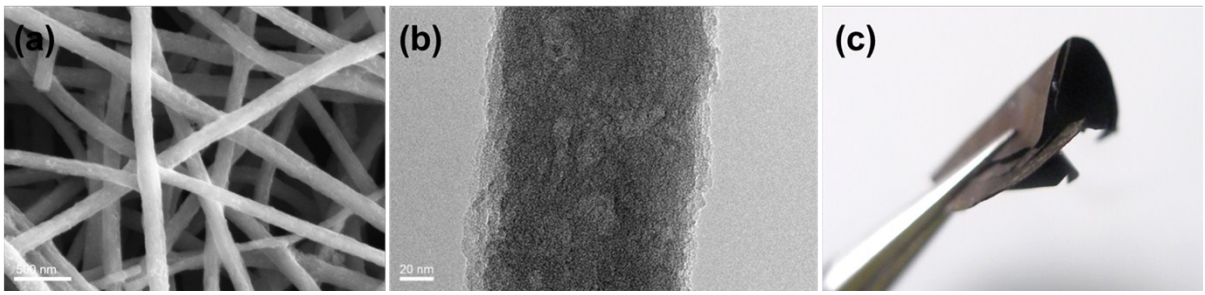

Fig. S12 a) SEM image, b) TEM image, and c) digital photograph of FCNF-3/4 following the rate cycles. After the rate cycles, the FCNF-3/4 electrode retains its original fibrous 3D network structure, and the fiber maintains its porous structure. More interestingly, the FCNF-3/4 electrode exhibits flexibility after the rate cycles, which is essential to ensure good electrochemical performance during continual deformation.

Table S2. Comparison of the electrochemical and mechanical performances of the FCNFs and previously reported flexible anode materials for lithium-ion batteries.

Sample	Substrate	Active materials	Electrode fabrication	Mechanical property	Half cell		Fully flexible Li-ion battery	
					Capacity/ mAh g^{-1} (Cycle number)	Current density /mA g^{-1}	Capacity/ mAh g^{-1} (Cycle number)	Current density /mA g^{-1}
SnO_x:ZnO/ CNF[6]	ES-CNF	SnO_x:ZnO (3:1)	Binder- and conductive-additive-free	Flexible	963 (55^{th})	100	N/A	N/A
SnO_2/ NCNF[8]	ES-CNF	SnO_2	PVDF, super P, and Cu foil	Flexible	754 (300^{th})	1000	N/A	N/A
TiO_2(B)/ ACF[11]	ES-CNF	TiO_2	Binder- and conductive-additive-free	Flexible	200 (1000^{th})	335	N/A	N/A
MnO-CNF[12]	ES-CNF	MnO	Binder- and conductive-additive-free	Flexible	923 (100^{th})	123	N/A	N/A
V_2O_3/CNF [13]	ES-CNF	V_2O_3	Binder- and conductive-additive-free	Flexible	500 (100^{th})	100	N/A	N/A
Fe_2O_3/SnO_x/ CNF[14]	ES-CNF	Fe_2O_3/ SnO_x	Binder- and conductive-additive-free	Flexible	756 (55^{th})	100	N/A	N/A
In_2O_3/ FUACNFF [15]	ES-CNF	In_2O_3	Binder- and conductive-additive-free	Flexible	545.6 (500^{th})	200	661 (20^{th})	200
Fe_2O_3@BC-CNF[16]	Bacterial Cellulose (BC)-CNF	Fe_2O_3	Binder- and conductive-additive-free	Flexible	755 (80^{th})	100	N/A	N/A
MoS_2-cBC[17]	BC-CNF	MoS_2	Binder- and conductive-additive-free	Flexible	581 (1000^{th})	1000	N/A	N/A
NGP–Fe_3O_4[18]	CNF, and GO	Fe_3O_4	Binder- and conductive-additive-free	Flexible	1427.5 (100^{th})	1000	N/A	N/A
CNT fabric@Si [19]	CNT fabric	Si	Binder-, conductive-additive-, and metal-current-collector-free	Flexible	494 (150^{th})	0.2C	N/A	N/A
MoS_2 /carbon cloth[20]	Carbon cloth	MoS_2	Metal foil	Bendable	~3 mAh cm^{-2} (30^{th})	0.15 mA cm^{-2}	~1.41 mAh cm^{-2} (15^{th})	0.15 mA cm^{-2}
$ZnCo_2O_4$/	Carbon	$ZnCo_2O_4$	Binder-, conductive-	Flexible	1200	200	1314	200

carbon cloth [21]	cloth		additive-, and metal-current-collector-free		(160^{th})		(40^{th})	
CNT/LTO [22]	CNT	$Li_4Ti_5O_{12}$	PVDF and super P	Flexible	140 (300^{th})	0.2C	120 (20^{th})	0.2C
TiO_2-PEDOT:PSS-CNT[23]	CNT	TiO_2	PVDF and Cu foil	Flexible	230 (100^{th})	0.33C	N/A	N/A
FCNF-3/4 (present work)	**ES-CNF**	**-**	**Binder-, conductive-additive-, and metal-current-collector-free**	**Highly foldable**	**630 (100^{th})**	**200**	**572 (1^{st})**	**100**
FCNF-1/2 (present work)	**ES-CNF**	**-**	**Binder-, conductive-additive-, and metal-current-collector-free**	**Highly foldable**	**287 (100^{th})**	**200**	**N/A**	**N/A**

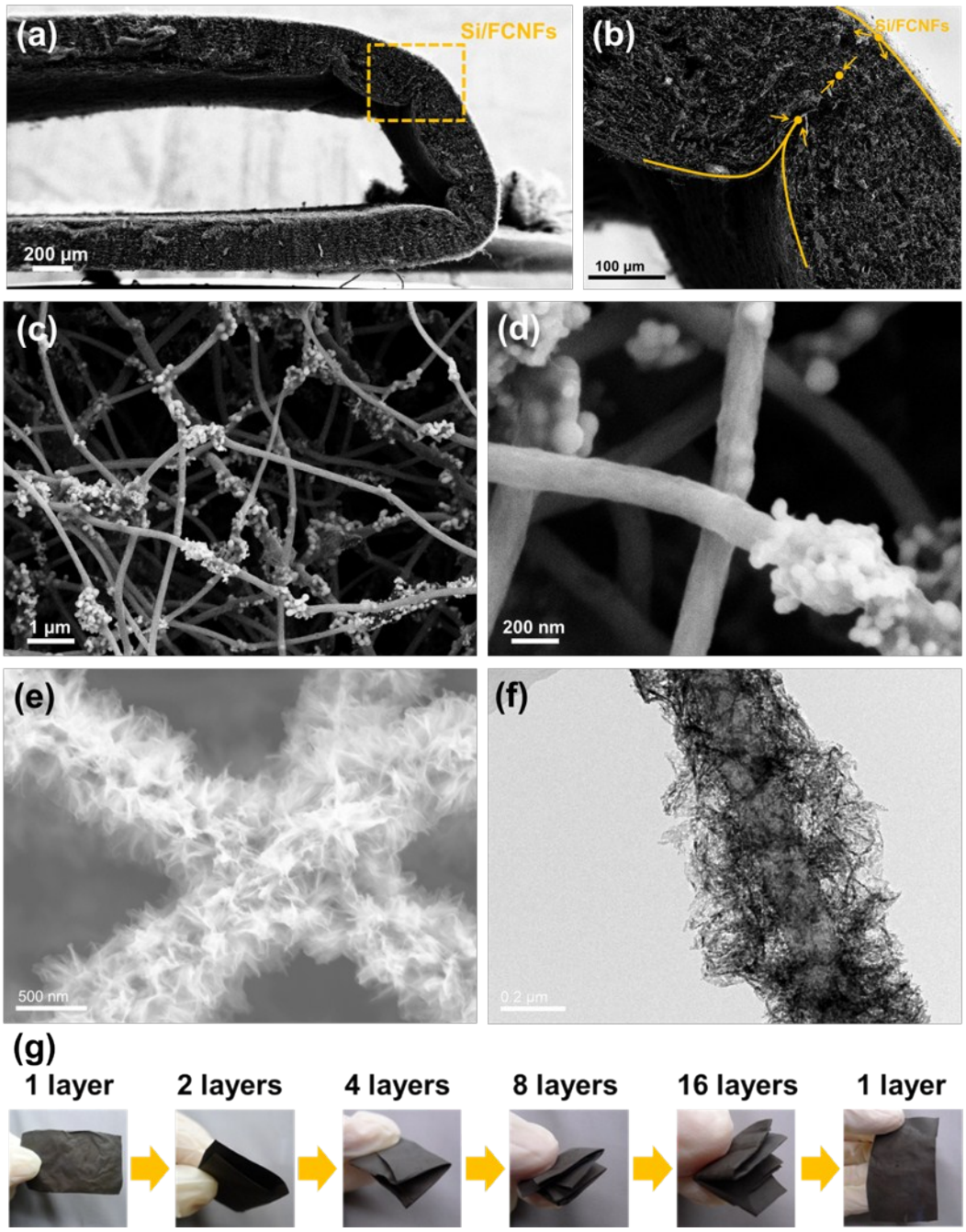

Fig. S13 a–d) SEM images with different magnifications of a flexible Si/FCNF fabricated via a typical electrospinning–carbonization process.[24] The Si/FCNF maintains its integrity without cracking when bent 180°, although its thickness can be up to 250 nm. e) SEM image of a Zn–Co precursor/FCNF fabricated using a typical solvothermal method,[25,26] f) TEM image of $Zn_xCo_{3-x}O_4$/FCNF, and g) digital photographs of $Zn_xCo_{3-x}O_4$/FCNF folded up to four times.

Fig. S14 Digital photograph of the full as-obtained foldable LCO-FCNF battery.

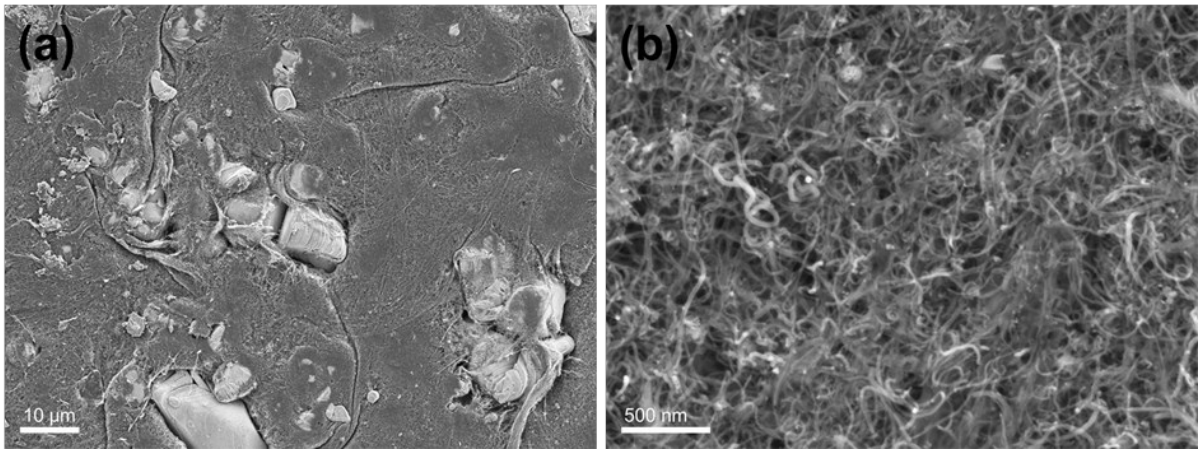

Fig. S15 a, b) SEM images with different magnifications of a commercial, flexible LCO/CNT cathode.

Reference

1 O. K. Park, S. Lee, H. I. Joh, J. K. Kim, P. H. Kang, J. H. Lee, B. C. Ku, *Polymer* 2012, **53**, 2168-2174.

2 W. Li, M. Li, M. Wang, L. Zeng, Y. Yu, *Nano Energy* 2015, **13**, 693-971.

3 Y. Liu, J. Zhou, L. Chen, P. Zhang, W. Fu, H. Zhao, Y. Ma, X. Pan, Z. Zhang, W. Han, E. Xie, *ACS Appl. Mater. Interfaces* 2015, **7**, 23515-23520.

4 G. Zhou, T. Xiong, S. Jiang, S. Jian, Z. Zhou, H. Hou, *Mater. Lett.* 2016, **165**, 91-94.

5 S. Kim, B. Bajaj, C. K. Byun, S. J. Kwon, H. I. Joh, K. B. Yi, S. Lee, *Appl. Surf. Sci.* 2014, **320**, 218-224.

6 B. N. Joshi, S. An, H. S. Jo, K. Y. Song, H. G. Park, S. Hwang, S. S. Al-Deyab, W. Y. Yoon, S. S. Yoon, *ACS Appl. Mater. Interfaces* 2016, **8**, 9446-9453.

7 J. Ge, Y. Qu, L. Cao, F. Wang, L. Dou, J. Yu, B. Ding, *J. Mater. Chem. A* 2016, **4**, 7795-7804.

8 L. Xia, S. Wang, G. Liu, L. Ding, D. Li, H. Wang, S. Qiao, *Small* 2016, **12**, 853-859.

9 S. Wang, L. Xia, L. Yu, L. Zhang, H. Wang, X. W. D. Lou, *Adv. Energy Mater.* 2015, 1502217.

10 Q. Liu, Y. Wang, L. Dai, J. Yao, *Adv. Mater.* 2016, **28**, 3000-3006.

11 S. Liu, Z. Wang, C. Yu, H. B. Wu, G. Wang, Q. Dong, J. Qiu, A. Eychmüller and X. W. Lou, *Adv. Mater.* 2013, **25**, 3462-3467.

12 E. Samuel, H. S. Jo, B. Joshi, S. An, H. G. Park, Y. Il Kim, W. Y. Yoon and S. S. Yoon, *Electrochim. Acta* 2017, **231**, 582-589.

13 S. Gao, D. Zhang, K. Zhu, J. A. Tang, Z. Gao, Y. Wei, G. Chen and Y. Gao, *J. Alloys Compd.* 2017, **702**, 13-19.

14 B. N. Joshi, S. An, Y. I. Kim, E. P. Samuel, K. Y. Song, I. W. Seong, S. S. Al-Deyab, M. T. Swihart, W. Y. Yoon and S. S. Yoon, *J. Alloys Compd.* 2017, **700**, 259-266.

15 J. Zhu, L. Chen, Z. Xu and B. Lu, *Nano Energy* 2015, **12**, 339-346.

16 Y. Wan, Z. Yang, G. Xiong, R. Guo, Z. Liu and H. Luo, *J. Power Sources*, 2015, **294**, 414-419.

17 F. Zhang, Y. Tang, Y. Yang, X. Zhang and C. S. Lee, *Electrochim. Acta* 2016, **211**, 404-410.

18 X. Huang, B. Sun, S. Chen and G. Wang, *Chem. - Asian J.* 2014, **9**, 206-211.

19 K. Evanoff, J. Benson, M. Schauer, I. Kovalenko, D. Lashmore, W. J. Ready and G. Yushin, *ACS Nano* 2012, **6**, 9837-9845.

20 H. Yu, C. Zhu, K. Zhang, Y. Chen, C. Li, P. Gao, P. Yang and Q. Ouyang, *J. Mater. Chem. A* 2014, **2**, 4551-4557.

21 B. Liu, J. Zhang, X. Wang, G. Chen, D. Chen, C. Zhou and G. Shen, *Nano Lett.* 2012, **12**, 3005-3011.

22 L. Hu, H. Wu, F. La Mantia, Y. Yang and Y. Cui, *ACS Nano* 2010, **4**, 5843-5848.

23 Z. Chen, J. W. F. To, C. Wang, Z. Lu, N. Liu, A. Chortos, L. Pan, F. Wei, Y. Cui and Z. Bao, *Adv. Energy Mater.* 2014, **4**, 1400207.

24 Y. Chen, Y. Hu, Z. Shen, R. Chen, X. He, X. Zhang, Y. Li, K. Wu, *J. Power Sources* 2017, **342**, 467-475.

25 R. Chen, Y. Hu, Z. Shen, Y. Chen, X. He, X. Zhang, Y. Zhang, *ACS Appl. Mater. Interfaces* 2016, **8**, 2591-2599.

26 Q. Fan, W. Liu, Z. Weng, Y. Sun, H. Wang, *J. Am. Chem. Soc.* 2015, **137**, 12946-12953.